

**Monte Carlo simulations of single and coupled synthetic molecular motors**C.-M. Chen<sup>1,\*</sup> and M. Zuckermann<sup>2</sup><sup>1</sup>*Department of Physics, National Taiwan Normal University, Taipei, Taiwan*<sup>2</sup>*Department of Physics and IRMACS Centre, Simon Fraser University, Canada*

(Received 19 May 2012; revised manuscript received 10 September 2012; published 5 November 2012)

We use a minimal model to study the processive motion of coupled synthetic molecular motors along a DNA track and we present data from Monte Carlo (MC) computer simulations based on this model. The model was originally proposed by Bromley *et al.* [HFSP J. **3**, 204 (2009)] for studying the properties of a synthetic protein motor, the “Tumbleweed” (TW), and involves rigid Y-shaped motors diffusively rotating along the track while controlled by a series of periodically injected ligand pulses into the solution. The advantage of the model is that it mimics the mechanical properties of the TW motor in detail. Both the average first passage time which measures the diffusive motion of the motors, and the average dwell time on the track which measures their processivity are investigated by varying the parameters of the model. The latter includes ligand concentration and the range and strength of the binding interaction between motors and the track. In particular, it is of experimental interest to study the dependence of these dynamic time scales of the motors on the ligand concentration. Single rigid TW motors were first studied since no previous MC simulations of these motors have been performed. We first studied single motors for which we found a logarithmic decrease of the average first passage time and a logarithmic increase of the average dwell time with increasing ligand concentration. For two coupled motors, the dependence on ligand concentration is still logarithmic for the average first passage time but becomes linear for the average dwell time. This suggests a much greater stability in the processive motion of coupled motors as compared to single motors in the limit of large ligand concentration. By increasing the number of coupled motors,  $m$ , it was found that the average first passage time of the coupled motors only increases slowly with  $m$  while the average dwell time increases exponentially with  $m$ . Thus the stability of coupled motors on the track can be considerably enhanced by their cooperative motion.

DOI: [10.1103/PhysRevE.86.051905](https://doi.org/10.1103/PhysRevE.86.051905)

PACS number(s): 87.85.gj, 07.05.Tp, 87.15.hj

**I. INTRODUCTION**

Biological molecular motors are mechanoenzymes which transduce chemical energy into mechanical energy in order to perform a plethora of biological tasks [1–4]. These include cellular transport, cell division, cell migration, DNA replication, and many other phenomena. For example, bipedal cytoskeletal stepping motors such as kinesin and myosin V are responsible for a variety of cellular tasks such as the transportation of organelles and vesicles containing nutrients in neurons. These autonomous motors are powered by adenosine-5'-triphosphate (ATP) and they undergo both processive and directed motion along one-dimensional tracks composed of protein fibers such as microtubules and actin. Biological nanomotors walking on a track often function in groups and have been characterized by Leibler and Huse [5] as either “rowers” or “porters.” These authors describe their properties in terms of a single comprehensive model. Their conclusion is that porters, which are responsible for carrying loads, spend most of their time bound to the track and, as such, can achieve their maximum velocity on their own or in small groups. On the other hand, rowers such as monomeric muscle myosin spend most of their time cycling between weakly bound and unbound states while waiting for a power stroke. This reduces friction and Leibler and Huse propose that such motors work best in large uncorrelated groups. Dimeric bipedal stepping motors and

the synthetic nanomotor concept examined in this work are examples of porters.

Several authors [6–8] have examined situations where biological molecular motors of the porter category perform tasks in groups of several coupled motor units either cooperatively or competitively. Klumpp and Lipowsky [6] examine the forces required for cooperative cargo transport by several processive cytoskeletal motors and point out that the force generated by a single motor of this type is only of the order of a few piconewtons. They state that this is not sufficient for fast transport of loads such as large organelles, for example. For this case they show that several motors are required. Stukalin *et al.* [7] use a discrete stochastic model based on chemical rate constants for two energetically coupled motors with each motor moving on its own track. They show that the composite motor is both faster and more efficient than for single motors and they successfully apply their model to data for recBCD helicase motors and state that their theory is quite general. Driver *et al.* [8] also use a discrete stochastic model to represent two coupled kinesin-1 motors moving on the same microtubule track. The model is again based on chemical rate constants which describe the individual motors as harmonic springs which can bind to and unbind from the track at one end and are affected by both assisting and opposing loads at the other end. These authors study the effect of deformations in mechanical linkages in coupled motors using this model and show that the advantage in linking stepping motors may be smaller than predicted by previous models. In this work we use a minimal mechanical model of a synthetic protein motor which partially mimics the behavior of cytoskeletal motors to examine the effect of coupling identical motors.

---

\*Present address: Department of Physics, 88 Sec. 4 Ting-Chou Rd. Taipei, Taiwan 116; cchen@phy.ntnu.edu.tw

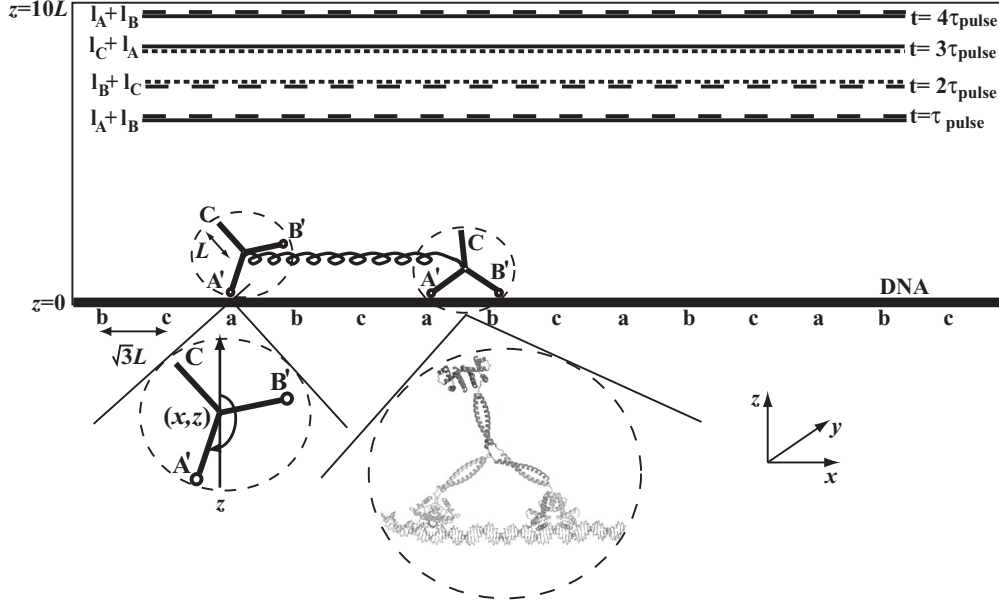


FIG. 1. Schematic representation of the setup used in our Monte Carlo simulations to investigate the motion of coupled TW motors inside a nanochannel. The ligand pulses are represented by solid lines for  $I_A$ , long dashed lines for  $I_B$ , and short dashed lines for  $I_C$ , and the time sequence of ligand pulses is denoted by  $t = \tau_{\text{pulse}}, 2\tau_{\text{pulse}}, 3\tau_{\text{pulse}}, \dots$ . The enlargements in the representation of the coupled motors show the molecular structure of a single Y-motor bound to DNA (see Ref. [10]) and a two-dimensional representation of a Y-motor as specified by its hub position and a rotational angle.

Biological nanomotors have inspired several research groups to design and construct synthetic molecular nanomotors whose energy sources are either chemical or optical. Recently Bromley *et al.* [9] introduced a novel concept for a synthetic molecular motor, the Tumbleweed (TW), which is constructed from nonmotor protein building blocks. The TW is designed to be a protein motor moving on a synthesized DNA track controlled by three ligand gated repressor proteins. Binding to and dissociation from the track is controlled by three ligand pulses per time period, resulting in directional motion along the track. The repressor proteins (feet) are each connected to a small flexible oligopeptide hub by a rigid coiled coil of length  $\sim 5$  nm. The connection between the repressors and their respective coiled coils is also flexible. The details of the TW are shown in Fig. 1. In a second TW article, Kuwada *et al.* [10] simulated a minimal model of the TW called the “Y-motor” in order to determine how design details could be tuned to optimize motor performance. The aim of the work of Kuwada *et al.* was to investigate synthetic protein motors both theoretically and experimentally in order to examine the basic operations of biological molecular motors in a controlled manner.

The purpose of our work is to elicit the properties of coupled synthetic protein motors with a view to understanding the basic operations of the multimotor complexes found in biology. To this purpose, we use the Y-motor model for the TW of Kuwada *et al.* and for simplicity we take a version of the Y-motor which is completely rigid and exactly matches the specifications of the track. The Y-motor model is described in detail in Sec. II and the metropolis Monte Carlo (MC) used in this work is presented in Sec. III. Section IV contains both simulation results and the discussion. In Sec. IV A, we extend the analysis of Kuwada *et al.* by simulating the rigid Y-motor in detail

so as to allow for a comparison with the simulation results for Y-motors coupled by rigid chemical bonds in Sec. IV B. Particular emphasis is placed on the average first passage time and motor processivity. Here the “first passage time”  $t_{\text{FPT}}$  is defined as the time between the release of the lagging foot of the motor and the binding of the leading foot to the track once the ligand pulse has been switched [10]. The average first passage time  $\tau_{\text{FPT}}$ , which is a measure of the time taken for the diffusion step of the motor, is defined to be the arithmetic mean of the values of first passage times which we calculate from MC simulations. The processivity of the motor is measured by the average dwell time  $\tau_{\text{dwell}}$ , this being the arithmetic mean of the dwell time  $t_{\text{dwell}}$  during which the motor remains bound to the track with no complete dissociation. Section V concludes the article with a summary of the main results and suggestions for further work.

## II. MODEL

In the present study, we begin by using the coarse-grained Y-motor model for a rigid TW [9–11] in conjunction with the metropolis Monte Carlo method for the simulation of its processive and directional motion along a DNA track. As shown in Fig. 1, the rigid Y-motor has three legs (coiled coil plus repressor) and the length of each leg ( $L = 7$  nm) was chosen to match the length of the appropriate protein components. Each foot is taken to be a different ligand-gated, DNA-binding repressor protein that interacts specifically and controllably with a DNA track [9]. Note that repressor proteins are allosteric proteins. Ligand-repressor binding enhances the affinity of the repressors to bind to DNA specifically by either conformational change in the repressors themselves or by modifying the electrostatic potential between the repressor

and the DNA backbone. It has been shown that the binding affinity of repressors to DNA increases  $100 \sim 1000$  fold in the presence of excess ligand [12,13]. The repressors, therefore, in the first approximation only bind to the operator sequence of base pairs (specific binding site) on the DNA track during a ligand pulse and dissociate rapidly after the removal of bulk ligand.

We estimate the probability  $P_{\text{bound}}$  of a ligand binding to the corresponding repressor by using a lattice model of  $N$  such ligands in solution, represented as a lattice of  $\Omega$  boxes and one receptor. We define two macrostates, the holo-state (H) for which the appropriate ligand is bound to the repressor and the apo-state (A) for which no ligand is bound to the repressor [11]. We write the energy difference between these two states as  $\Delta\varepsilon = \varepsilon_{\text{bound}} - \varepsilon_{\text{unbound}}$ . A straightforward calculation gives the probability of the bound state as

$$P_{\text{bound}} = \frac{\frac{N}{\Omega} e^{-\beta\Delta\varepsilon}}{1 + \frac{N}{\Omega} e^{-\beta\Delta\varepsilon}} = \frac{\frac{[N]}{K_d}}{1 + \frac{[N]}{K_d}}, \quad (1)$$

where  $[N] \equiv N/(\Omega v)$  is the ligand concentration,  $v$  is the volume of each box,  $\beta^{-1} \equiv k_B T$  is the thermal energy (about 4 pN nm at room temperature), and  $K_d = e^{\beta\Delta\varepsilon}/v$  is the equilibrium dissociation constant. Alternatively, the probability given by Eq. (1) can be derived by the law of mass action (LMA). Let  $[H]$  be the concentration of the repressor protein in the holo-state, let  $[A]$  be the concentration of the same repressor in the apo-state, and let  $[N]$  be the concentration of the corresponding ligand (L). From the LMA for the ligand binding process  $A + L \leftrightarrow H$ , we have the dissociation constant  $K_d = [A][N]/[H]$ . Here  $K_d = k_{\text{off}}/k_{\text{on}}$ , where  $k_{\text{on}}$  and  $k_{\text{off}}$  are the rate constants for ligand binding to and ligand unbinding from the repressor protein, respectively. Since the probability that the repressor is in the holo-state is  $P_{\text{bound}} = [H]/([A] + [H])$ , by substituting for  $[A]$  and  $[H]$ , we derive the probability of the bound state as  $P_{\text{bound}} = [N]/(K_d + [N]) = [N]k_{\text{on}}/(k_{\text{off}} + [N]k_{\text{on}})$ . A full treatment of rate constants and time scales for the TW in terms of holo- and apo-states can be found in Ref. [11].

A repressor can bind to the DNA track through a specific interaction to the corresponding operator sequence during the appropriate ligand pulse if it is in the holo-state or through a nonspecific interaction to the DNA track. In vitro experiments have shown that there exists a large difference between the specific and nonspecific equilibrium constants, about  $10^{-10} : 10^{-4}$  [14]. Equivalently, the specific interaction is stronger than the nonspecific interaction by an amount of  $13.8 k_B T$ . We therefore neglect the nonspecific interaction in this study. The specific interaction between a repressor  $i$  and its corresponding operator sequence [10] is modeled by a Gaussian potential function

$$V_{\text{SB}}(r_i) = \begin{cases} -V_0 \exp(-r_i^2/\xi^2) & \text{repressor in the holo - state} \\ 0 & \text{repressor in the apo - state.} \end{cases} \quad (2)$$

Here  $V_0$  is the interaction strength (in units of  $k_B T$ ),  $\xi$  is the effective range of interaction (in units of  $L$ ), and  $r_i$  is the distance between the repressor  $i$  and its nearest corresponding operator sequence on the track (in units of  $L$ ).

By properly choosing the three repressors (A, B, and C) on the feet of a TW motor and the operator sequences ( $a$ ,  $b$ , and  $c$ ) along the DNA track, it is possible to control the motion of the motor by changing the bulk concentration of the corresponding ligand ( $l_A$ ,  $l_B$ , and  $l_C$ ). For example, consider a DNA track with an operator sequence ( $a, b, c, a, b, c, \dots$ ) and the distance between two operator sequences is set to  $\sqrt{3}L$ . When the bulk solution contains a time series of ligand ( $l_A + l_B, l_B + l_C, l_C + l_A, l_A + l_B, \dots$ ), the TW motor will be driven toward the right-hand side of the DNA track by this time changing ligand concentration.

The protocol for binding is as follows: Consider, for example, the pulse sequence ( $l_A + l_B, l_B + l_C$ ). When the pulse is switched from the earlier pulse to the latter one, the lagging foot A is immediately released as the specific binding potential [Eq. (2)] for its binding sites  $a$  is switched off ( $V_0 \rightarrow 0$ ). The specific binding potential for binding sites  $b$ , however, is retained so that B' can remain bound. In addition, the binding potential for binding sites  $c$  is switched on so that the leading foot C' is able to bind during the pulse time for ligand pulse ( $l_B + l_C$ ). Here we use A', B', and C' to denote the ligand-bound state of repressors A, B, and C, respectively. The characteristic time for unbinding of a foot is zero while that for binding is controlled by the value of  $V_0$ , which is made high enough to ensure binding when a ligand is bound to the foot. The specific binding potential of Eq. (2) controls binding when it has been switched on.

As stated in the introduction, the main purpose of this study is to investigate the constrained motion of  $m$  coupled TW motors along the DNA track caused by the time series of ligand changes. These TW motors are constrained through connections between their hubs by an elastic polymer chain or a more rigid helix. The elastic energy associated with this connection is modeled by the following harmonic interaction:

$$V_{\text{el}} = \sum_{j=1}^{m-1} \frac{1}{2} k (l_{j,j+1} - 3\sqrt{3}L)^2, \quad (3)$$

where  $k$  is a spring constant and  $l_{j,j+1}$  is the hub distance between motors  $j$  and  $j+1$ . The total energy of  $m$  coupled motors can then be expressed as follows:

$$E = V_{\text{el}} + \sum_{j=1}^m \sum_{i=1}^3 V_{\text{SB}}^j(r_i). \quad (4)$$

### III. SIMULATION METHOD

The motion of single and coupled Y-motors in our Monte Carlo simulations takes place inside a nanochannel, as schematically illustrated in Fig. 1. The nanochannel has no limit in the  $x$  direction, while hard wall boundary conditions are imposed in the  $z$  direction ( $0 \leq z \leq 70$  nm) in the case of two-dimensional (2D) simulations, and in both the  $y$  and  $z$  directions ( $-70 \text{ nm} \leq y \leq 70 \text{ nm}$ ) for three-dimensional (3D) simulations. The DNA track is grafted on the lower surface ( $z = 0$ ) in the nanochannel and has a periodic series of operator sequences ( $a, b, c, a, b, c, \dots$ ) along the  $x$  axis. For rigid motors, if the repressors and the hub are strongly linked, the rotation of motors is preferentially along the DNA track due

to the binding of repressors to the operator sequences on the track. In this case, the processive motion of the motors along the track can be investigated by simplified 2D simulations. However, if the repressors are linked to the hub by flexible loops, the motors can undergo 3D rotations along the track. 3D simulations are therefore more realistic in this case.

The coupled Y-motors were initially placed at a random position and they then were allowed to diffuse in the nanochannel. For the 2D simulations, each Y-motor was specified by the position  $(x, z)$  of its hub, the rotational angle  $\theta$ , and the state of three repressors. For the 3D simulations, each Y-motor was specified by the hub position  $(x, y, z)$ , three Euler angles  $(\theta_1, \theta_2, \theta_3)$ , and the state of three repressors. In our Monte Carlo simulations, the binding between the repressors of each Y-motor and their corresponding ligands was first investigated for the bulk concentration of ligands and the probability of binding given by Eq. (1). The instantaneous motion of each Y-motor was simulated by an attempted movement of its hub with an arbitrary translation between zero and 0.05 nm and an arbitrary rotation between zero and 0.3 degrees. This move was accepted with probability  $w = \min[1, \exp(-\Delta\beta E)]$ , where  $\Delta E$  is the change of system energy in Eq. (4). In our simulations, unless otherwise specified, the parameter set is given by  $\xi = 0.71$  nm,  $V_0 = 100k_B T$  (400 pN nm),  $[N]/K_d = 100$ , and  $k = k_0 = 0.082$  pN/nm. The details of the units are given in the next section. After the coupled Y-motors first bind to the DNA track, they walk along the DNA track under the control of a time series of bulk ligand pulses. As shown in Fig. 1, this time series of ligand pulses ( $l_A, l_B, l_C$ ) is set to  $\{([N], [N], 0), (0, [N], [N]), ([N], 0, [N]), ([N], [N], 0), \dots\}$ , where  $[N]$  is the ligand concentration. The duration of each pulse ( $\tau_{\text{pulse}} = 2 \times 10^7$  MC steps) is the same in all our simulations and is taken to be longer than  $t_{\text{FPT}}$  for a ligand-bound repressor to find its corresponding operator sequence on the DNA track by rotational diffusion after the change in ligand composition. For example, in the presence of ligands  $l_A$  and  $l_B$  in the solution, the probability that the repressors will have ligands bound to them is given by Eq. (1). When the ligand pulse is switched to  $l_B + l_C$ , the repressor  $A'$  will dissociate from the track due to the unbinding of  $l_A$ , while the repressor  $B'$  still remains bound to the track. A transition from C to  $C'$  is assumed to occur directly with the probability  $P_{\text{bound}}$  after switching the ligand pulse from  $l_A + l_B$  to  $l_B + l_C$ , and the coupled motors would then move one step in the positive  $x$  direction. With the above time series of ligand pulses, the coupled Y-motors move three steps ( $3\sqrt{3}L$ ) ahead in a complete cycle. For simplicity, we assume a step function profile of ligand concentration. We note that hydrodynamic flow will affect the rotational diffusion of the motors more significantly in 3D simulations than in 2D simulations. However, in the present study, we have neglected hydrodynamic effects in order to simplify the simulations.

Monte Carlo simulations of nonequilibrium processes can be interpreted in terms of the time evolution of a Markov chain, since the correlations between successive configurations in the Markov chain can be understood from a dynamic interpretation of the Monte-Carlo process in terms of a master equation describing a dynamic model with stochastic kinetics [15–18]. However, an absolute measure of physical time is not provided

in this approach. We calibrate the physical time in Monte Carlo simulations by measuring the self-diffusion constant of a Y-motor in solution from both Monte Carlo simulations and Langevin dynamics. The details of the Langevin dynamics method together with the values of the parameters used in the Langevin dynamics simulations and those of the calculated diffusion constants are given in the Appendix. In detail, measurement of the self-diffusion constant using Langevin dynamics,  $D_{\text{LD}}$ , and calculation of the mean square displacement per MC step,  $\langle \Delta r^2 \rangle_{\text{MC}}$ , allows us to obtain the physical time per MC as follows:

$$\tau = \frac{\langle \Delta r^2 \rangle_{\text{MC}}}{D_{\text{LD}}}, \quad (5)$$

We found that, for our model, each MC step is 25 ps for 2D MC simulations and is 27 ps for 3D MC simulations.

## IV. RESULTS AND DISCUSSION

### A. Single Y-motors

We began our investigation of the processive motion of single and coupled Y-motors by first examining the processive behavior of single Y-motors. In particular, we calculated the average first passage time ( $\tau_{\text{FPT}}$ ) and the average dwell time ( $\tau_{\text{dwell}}$ ) of these motors on the DNA track under various conditions. The units of length and time used in this study were set as  $\{L, \text{MC step}\} = \{7 \text{ nm}, 25 \text{ ps}\}$ . In Fig. 2, we show three traces for the motion of both a single Y-motor [Fig. 2(a)] and two coupled motors [Fig. 2(b)], corresponding to  $V_0 = 100k_B T$  (400 pN nm),  $10k_B T$  (40 pN nm), and  $k_B T$  (4 pN nm), respectively. Trace I in Fig. 2(a) gives the calculated stepping data (i.e., the  $x$  coordinate) for the Y-motor's center of mass for  $V_0 = 100k_B T$ , demonstrating a perfectly processive motion of the single rigid Y-motor model along the DNA track provided  $\tau_{\text{pulse}}$  is long enough for the Y-motor to diffuse to the next binding site. For a lower binding potential ( $V_0 = 10k_B T$ ), the motion of the Y-motor along the track becomes less regular. In trace II of Fig. 2(a), the motor sometimes detaches from the track, particularly when the ligand pulse changes. At  $t = 500 \mu\text{s}$ , the Y-motor makes two backward steps; while at  $t = 5 \text{ ms}$ , it moves forward three steps. When the binding potential is weaker than the thermal energy, as shown in trace III of Fig. 2(a), the Y-motor diffuses in the nanochannel instead of walking along the track.

In Fig. 3, we show the distributions of the first passage time for  $\xi = 3.16$  nm, 2.24 nm, and 1.58 nm (a) and for 2D and 3D simulations (b). As inferred from Eq. (2), the motor takes a longer time to search for the binding site by diffusion for a smaller value of  $\xi$  and this search time is independent of  $\xi$  for small enough  $\xi$ . Indeed our MC simulations show that the value of  $\tau_{\text{FPT}}$  increases as  $\xi$  decreases and saturates for small  $\xi$  values [see Fig. 4(a)]. For the same reason, it can be seen in Fig. 3(a) that the fluctuations of the distributions of  $\tau_{\text{FPT}}$  decrease with  $\xi$ . In Fig. 3(b), we compare the distribution curves of  $\tau_{\text{FPT}}$  in 2D and 3D simulations. The overlap of these two distribution curves indicates similarity in the general behavior of the motor's processive motion along the DNA track in 2D and 3D simulations. However, the tail of the 3D distribution curve is slightly higher than that of the 2D

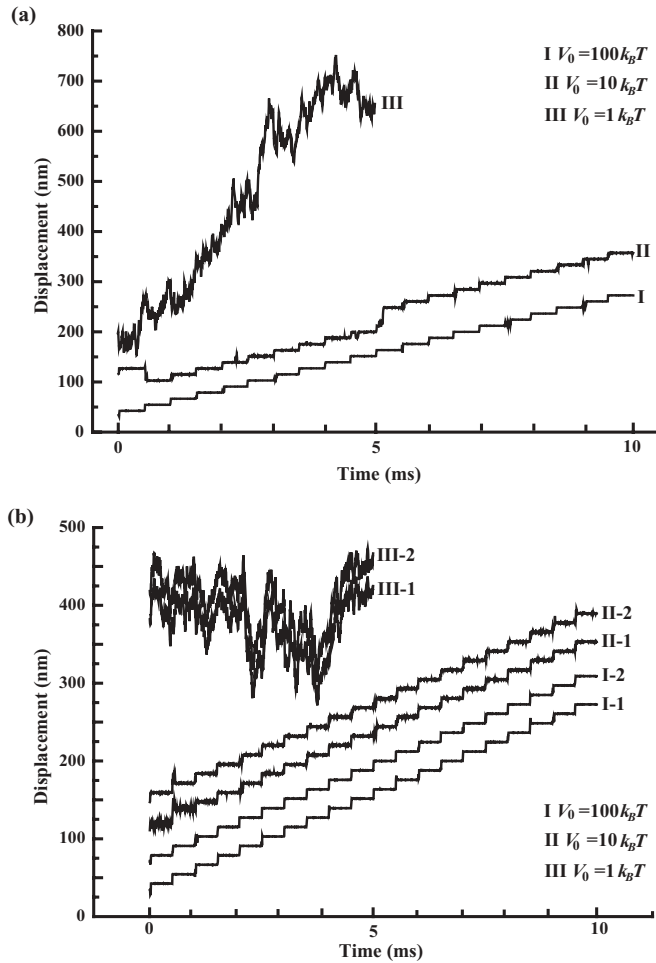


FIG. 2. Two-dimensional simulation results for the hub position of a single Y-motor (a) and coupled Y-motors (b).

distribution curve, implying slightly larger values of  $\tau_{\text{FPPT}}$  in 3D simulations. Since there is no significant difference between results from 2D and 3D simulations, we will focus on results from 2D simulations in the following discussion.

Figure 4(b) shows the average first passage time as a function of  $V_0$ . For  $V_0 > 10 k_B T$ , the average first passage time is almost a constant. During this process, one foot of the motor is tightly bound to the DNA track and  $\tau_{\text{FPPT}}$  is mainly determined by the rotational diffusion of the motor. For  $V_0 < 10 k_B T$  the value of  $\tau_{\text{FPPT}}$  increases exponentially as  $V_0$  decreases, as shown by the solid fitting curve. In this case, the motor undergoes both translational and rotational diffusion due to a weaker binding of repressors to the appropriate binding sequences on the DNA track, which increases the average first passage time. Figure 4(c) shows a logarithmic decrease of the average first passage time on ligand concentration  $[N]$ . In principle, larger values of  $[N]$  mainly stabilize the repressor binding onto the track, which leads to shorter search times for the next binding site by rotational diffusion. For  $[N]/K_d > 500$ , the probability of ligand binding to the repressors is 99.8% and the average first passage time decreases slightly with  $[N]$ . The experimental values of  $K_d$  for different repressors are as follows:  $K_d = 7 \mu\text{M}$  for PurR [19],  $200 \mu\text{M}$  for MetJ [20], and  $42 \mu\text{M}$  for TrpR [21]. A typical value of  $[N]/K_d$  used in

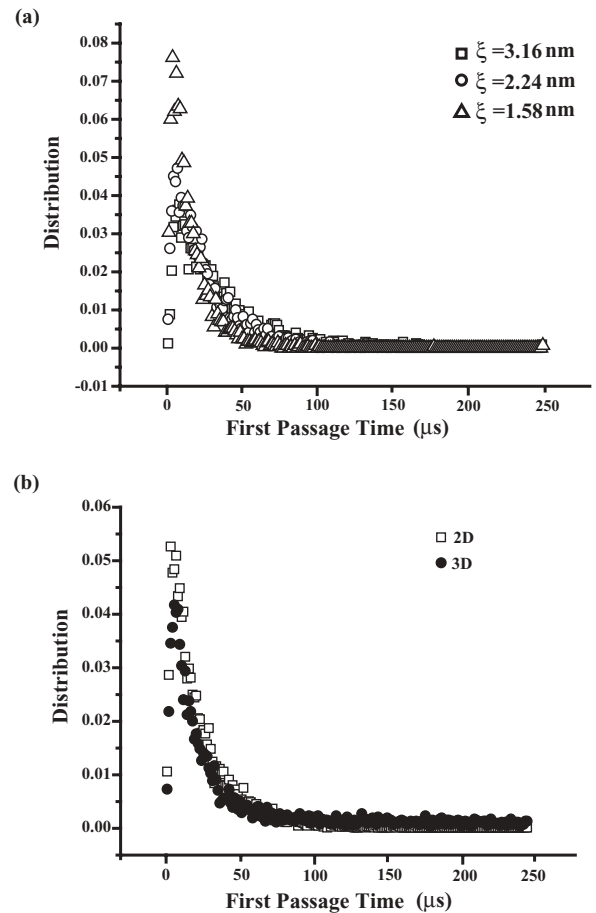


FIG. 3. First passage time distribution of a single Y-motor for various values of the effective range of interaction  $\xi$  (a) and for simulations in two and three dimensions (b).

our simulations is 100 [see Fig. 4(c)] and the equivalent ligand concentrations for this value are 0.7 mM for PurR, 20 mM for MetJ, and 4.2 mM for TrpR.

Two factors affect the value of  $\tau_{\text{dwell}}$ : the strength  $V_0$  of the binding potential and the effective range  $\xi$  of the binding interaction. For weaker binding, the average dwell time is relatively short due to early detachment of the motor from the track. On the other hand, a larger effective range of binding reduces the average first passage time and thus increases the average dwell time. The average dwell time of a single motor on the track as a function of  $\ln(V_0)$  and  $[N]/K_d$  is shown in Figs. 5(a) and 5(b), respectively. Figure 5(a) shows that the average dwell time increases exponentially with  $V_0$  initially and saturates for  $V_0 > 100 k_B T$ . The initial growth of  $\tau_{\text{dwell}}$  with  $V_0$  is exponential (solid line) as shown in the inset of Fig. 5(a). This is consistent with Maxwell-Boltzmann statistics, in which case the time of ligand binding to a repressor ( $\tau_{\text{lb}}$ ) is considerably longer than that of repressor binding to the track ( $\tau_{\text{dwell}}$ ). For larger values of  $V_0$ ,  $\tau_{\text{lb}}$  is comparable to the average value of  $\tau_{\text{dwell}}$  and the unbinding of the repressor from the track sometimes results from detachment of ligand from the repressor. For  $V_0 > 100 k_B T$ ,  $\tau_{\text{lb}} \ll \tau_{\text{dwell}}$  and the detachment of the motor from the track is mainly due to the unbinding of ligand from its bound foot. In this case, although the binding potential in Eq. (2) increases with  $V_0$ ,

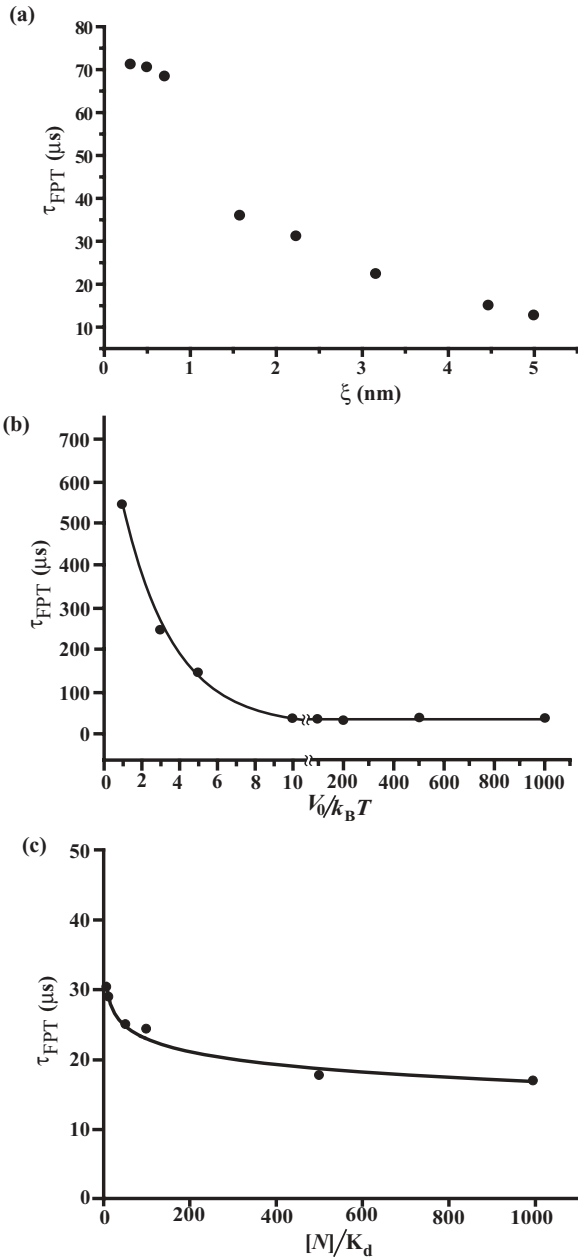


FIG. 4. Average first passage time of a two-dimensional Y-motor for various values of (a) the effective range of interaction  $\xi$ , (b) interaction strength  $V_0$ , and (c) ligand concentration  $[N]$ .

the average dwell time remains constant. Figure 5(b) shows that the average dwell time of the Y-motor on the track increases logarithmically with ligand concentration, since high ligand concentration facilitates repressor binding to the track. Figure 6 shows the average dwell time of the Y-motor on the track as a function of the range  $\xi$  of the binding potential [Fig. 6(a)] and the dwell time histograms for various values of  $\xi$  [Fig. 6(b)]. The average dwell time increases slightly with  $\xi$  for  $\xi < 2.21$  nm and  $\xi > 3.83$  nm, but decreases significantly with  $\xi$  for  $2.21 \text{ nm} < \xi < 3.83$  nm. As shown in the inset of Fig. 6, for  $\xi < 2.21$  nm, the binding potential is localized and strong. Increasing  $\xi$  increases the effective range of the binding interaction and thus increases the probability for the Y-motor to find the next binding site by rotational diffusion. Indeed, from

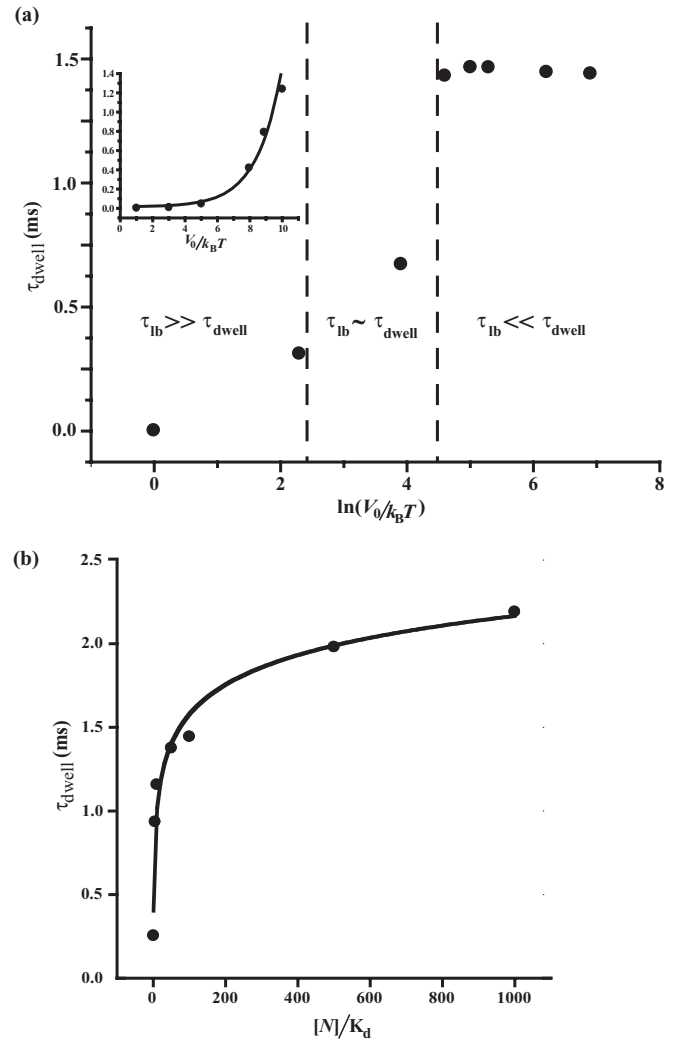


FIG. 5. Average dwell time of a two-dimensional Y-motor on a DNA track for various values of (a) interaction strength  $V_0$  and (b) ligand concentration  $[N]$ . In panel (a), the average dwell time has a different dependence on  $V_0$  in each of three regimes: In regime I  $\tau_{\text{lb}} \gg \tau_{\text{dwell}}$ , in regime II  $\tau_{\text{lb}} \sim \tau_{\text{dwell}}$ , and in regime III  $\tau_{\text{lb}} \ll \tau_{\text{dwell}}$ . The average dwell time increases exponentially with  $V_0$  in regime I as shown in the inset, while it is saturated in regime III. Regime II is a crossover from regime I to regime III.

the histogram of  $t_{\text{dwell}}$  for  $\xi = 0.49$  nm, 0.70 nm and 2.21 nm shown in Fig. 6(b), these distributions for  $t_{\text{dwell}} < 1.5$  ms are very similar, but the distribution for  $\xi = 2.21$  nm tends to be more populated for  $t_{\text{dwell}} > 2$  ms than that for  $\xi = 0.49$  or 0.70 nm. The rapid decrease of average dwell time with  $\xi$  for  $2.21 \text{ nm} < \xi < 3.83$  nm can also be understood from the distance dependence of the binding potential shown in the inset. In this case the binding potential of repressors to the track is less localized, leading to easier dissociation of the foot of the Y-motor from the track as  $\xi$  increases. The dwell time distribution for  $\xi = 3.13$  nm is substantially more populated at  $t_{\text{dwell}} < 1.5$  ms than that for  $\xi = 2.21$  nm. For  $\xi > 3.83$  nm, the foot of the Y-motor is seen to be bound to the track over a wider range of dwell times as  $\xi$  increases. The average dwell time therefore increases again with increasing  $\xi$ .

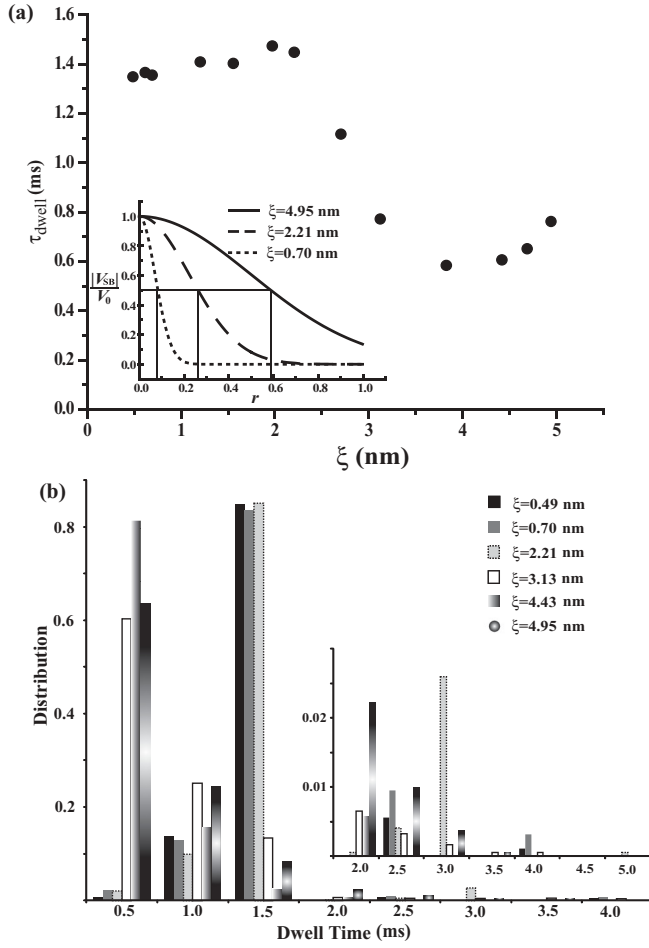


FIG. 6. Dependence of the average dwell time on the effective range of interaction  $\xi$  for a single Y-motor on a DNA track. (a) Average dwell time as a function of  $\xi$ . The inset shows the distance profile of the specific binding potential for  $\xi = 0.70, 2.21$ , and  $4.95$  nm. Here  $r$  is the distance between a foot of the Y-motor and the center of the binding site. (b) Dwell time histogram for several values of  $\xi$ . The inset is an enlargement of the histogram for dwell times between 2 and 5 ms.

### B. Coupled motors

Coupled molecular motors are used to transport cargo in a cooperative manner and are expected to have a small  $\tau_{\text{FPT}}$  and a large  $\tau_{\text{dwell}}$  [17,18] for practical applications. In order to investigate if this holds for synthetic coupled motors, we investigated the processive kinetics of coupled Y-motors along a DNA track by MC simulations. In our simulations, the coupling between Y-motors is implemented by the harmonic potential of Eq. (3). Figure 2(b) shows six traces of two coupled motors for  $V_0 = 100k_B T$ ,  $10k_B T$ , and  $k_B T$ , respectively. Traces I-1 and I-2 show the positions of the center of mass on the  $x$  axis for two coupled Y-motors with  $V_0 = 100k_B T$ , demonstrating perfectly processive motion for the coupled Y-motors along the track. For a lower binding potential ( $V_0 = 10k_B T$ ), thermal fluctuations became more significant but the two coupled Y-motors still remained on the track, as seen in traces II-1 and II-2. In many cases, one of the two coupled motors detached from the track but the other remained on the track. Therefore the processivity of the two

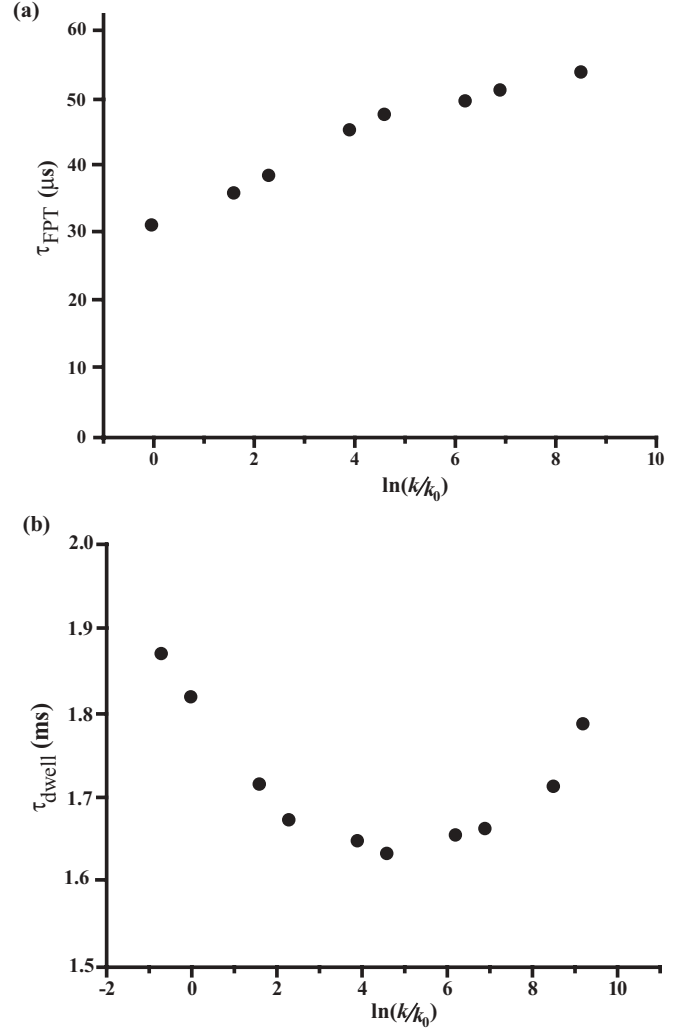


FIG. 7. Average first passage time (a) and average dwell time (b) for two coupled Y-motors walking on a DNA track as a function of the spring constant  $k$ . Here  $k_0 = 0.082$  pN/nm.

coupled Y-motors is more robust than that of a single Y-motor as seen in the trace II of Fig. 2(a). For an even lower binding potential ( $V_0 = k_B T$ ), as shown in traces III-1 and III-2 of Fig. 2(b), the motor diffuses in the box rather than walking on the track.

In Fig. 7, we show  $\tau_{\text{FPT}}$  [Fig. 7(a)] and  $\tau_{\text{dwell}}$  [Fig. 7(b)] for two coupled Y-motors walking along the track as a function of the elastic constant  $k$ . The coupling between Y-motors tends to suppress individual rotational diffusion of the individual Y-motors and enhance cooperative motion of the coupled Y-motors. As shown in Fig. 7(a), the average first passage time increases logarithmically with  $k$ . In the limit of rigid coupling between Y-motors, all Y-motors move in the same way in their search for the next binding site. The dependence of the average dwell time on  $k$ , as shown in Fig. 7(b), is, however, nontrivial. It decreases logarithmically with  $k$  initially, reaches a minimum at  $k/k_0 \cong 100$ , and then increases linearly with  $k$ . Near this minimum, the coupling potential is not strong enough to restrain any of the coupled Y-motors from dissociating from the track. As a result, the Y-motor which is detached from the track is likely to drag the bound Y-motor away from the track.

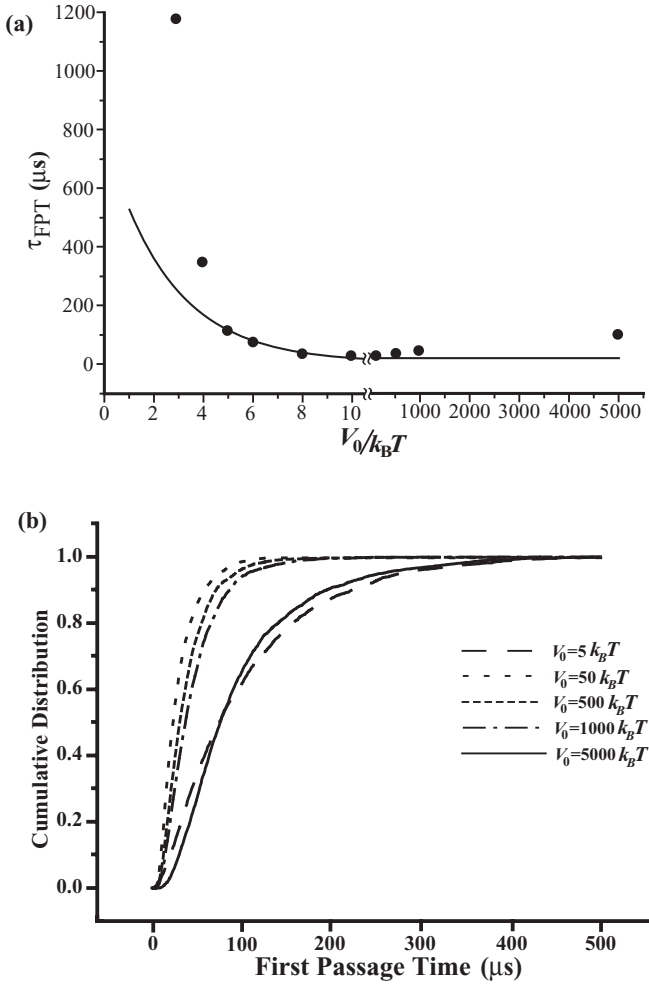


FIG. 8. Dependence of the average first passage time on the binding interaction strength  $V_0$  for two coupled Y-motors on a DNA track. (a) Average first passage time as a function of  $V_0$ . (b) Cumulative distribution of first passage times for several values of  $V_0$ . For comparison purposes, the solid line in (a) schematically shows the average first passage time of a single motor.

For large values of  $k$ , the detachment of a single Y-motor from the track is significantly suppressed by the coupling potential. Therefore, the average dwell time increases with  $k$  for  $k/k_0 > 100$ .

Figure 8 shows the average first passage time of two coupled Y-motors [Fig. 8(a)] and the cumulative distributions of first passage time [Fig. 8(b)] for  $V_0$  between  $5k_B T$  and  $5000k_B T$ . When  $V_0 < 50k_B T$ , the value of  $\tau_{\text{FPT}}$  increases as  $V_0$  decreases since the coupled Y-motors undergo both translational and rotational diffusion due to weaker binding of repressors to the DNA track. However, when  $V_0 > 50k_B T$ , the value of  $\tau_{\text{FPT}}$  increases linearly with  $V_0$ . This  $V_0$  dependence of  $\tau_{\text{FPT}}$  is quite different from that of a single Y-motor, as seen in Fig. 4(b) (schematically represented by the solid line). To understand the above  $V_0$  dependence of  $\tau_{\text{FPT}}$ , we display the cumulative distributions of first passage time for several values of  $V_0$  in Fig. 8(b). It is seen that the cumulative distributions of first passage time is highly populated (90%) at  $t_{\text{FPT}} < 62.5 \mu\text{s}$  for  $10k_B T \leq V_0 \leq 100k_B T$ , and becomes broader distributed for larger values of  $V_0$ . For  $V_0 = 5000k_B T$ , 90% cumulative

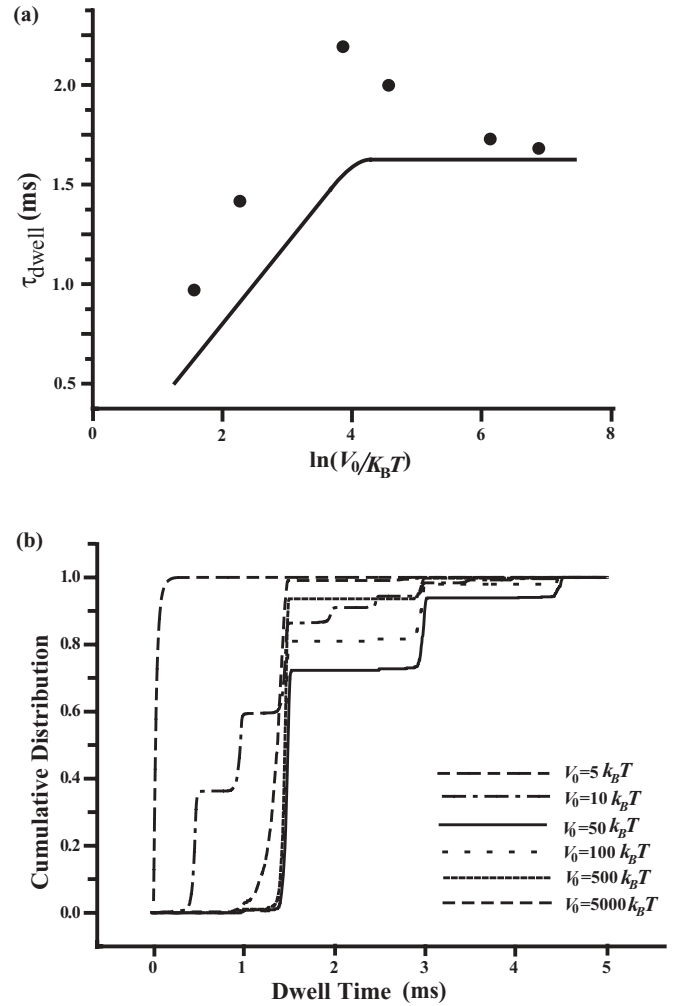


FIG. 9. Dependence of the average dwell time on the binding interaction strength  $V_0$  for the procession of two coupled Y-motors on the DNA track. (a) Average dwell time as a function of  $V_0$ . (b) Cumulative distribution of dwell times for several values of  $V_0$ . For comparison purposes, the solid line in (a) schematically shows the average dwell time of a single motor.

distribution occurs at about  $t_{\text{FPT}} = 200 \mu\text{s}$ . We conclude that, for a larger value of  $V_0$ , it is more likely for the coupled Y-motors to be trapped at a less favorable configuration for finding the next binding sites on the track, hence  $\tau_{\text{FPT}}$  increases with  $V_0$  for  $V_0 > 10k_B T$ . The comparison of  $\tau_{\text{FPT}}$  of a single motor with that of two coupled motors in Fig. 8(a) suggests that large binding strengths tend to slow down the processive motion of coupled motors. In Fig. 9, we show the average dwell time of two coupled Y-motors [Fig. 9(a)] and the cumulative distributions of dwell time [Fig. 9(b)] for  $V_0$  between  $5k_B T$  and  $5000k_B T$ . For  $V_0 < 50k_B T$ ,  $\tau_{\text{dwell}}$  decreases as  $V_0$  decreases due to a less strong binding with the track. When  $V_0 > 50k_B T$ , the average dwell time also decreases as  $V_0$  increases and saturates at about  $\tau_{\text{dwell}} = 1.5 \text{ ms}$ , which is quite different from the case of a single Y-motor [as schematically illustrated by the solid line in Fig. 9(a)]. The cumulative distribution in Fig. 9(b) shows that, for  $V_0 > 50k_B T$ , the dwell time of two coupled Y-motors are mostly populated at  $\tau_{\text{dwell}} = 1.5 \text{ ms}$ . However, for  $50k_B T \leq V_0 \leq 100k_B T$ , a significant portion of

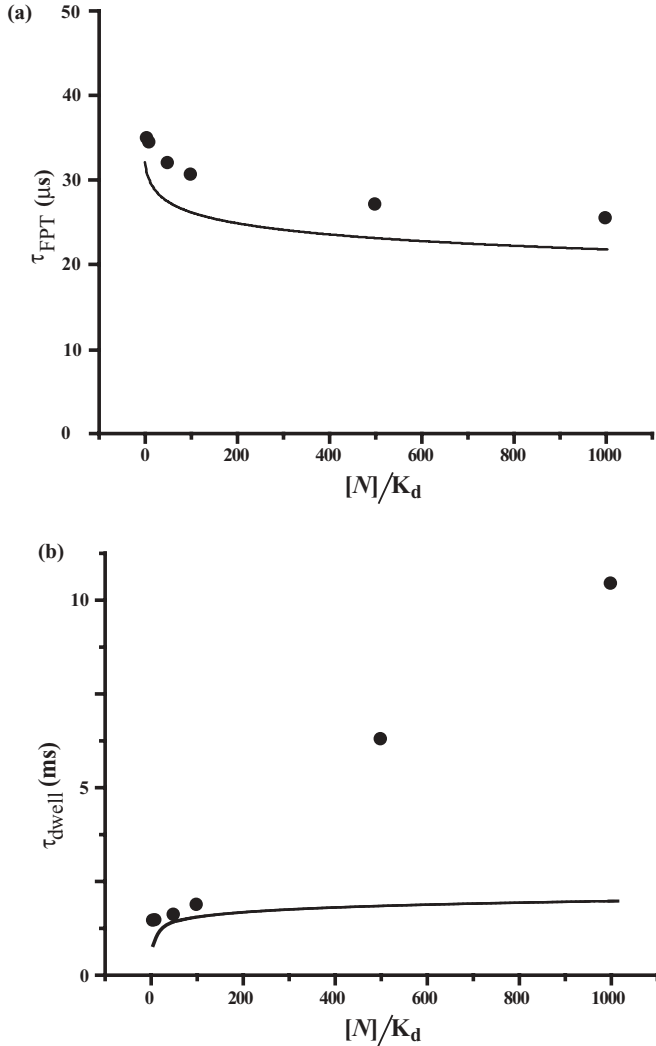


FIG. 10. Average first passage time (a) and average dwell time of two coupled Y-motors walking on a DNA track as a function of ligand concentration  $[N]$  (b). For comparison purposes, the solid lines in panels (a) and (b) schematically show the average first passage time and the average dwell time of a single motor, respectively.

the distribution of dwell times is observed at  $\tau_{\text{dwell}} = 3$  ms. This cooperative effect results from the fact that, for the two coupled Y-motors to detach from the track completely, both ligands bound to the two coupled Y-motors must unbind at the same time. The comparison of  $\tau_{\text{dwell}}$  of a single motor with that of two coupled motors in Fig. 9(a) suggests that the stability of the processive motion of the motors is not affected significantly by their coupling over a wide range of binding strengths.

In Fig. 10, we show the dependence of  $\tau_{\text{FPT}}$  [Fig. 10(a)] and  $\tau_{\text{dwell}}$  [Fig. 10(b)] on  $[N]/K_d$ . The average first passage time of two coupled Y-motors in Fig. 10(a) has a very similar logarithmic dependence on ligand concentration as that of a single Y-motor shown in Fig. 4(c) [solid line in Fig. 10(a)]. However, the average dwell time of two coupled Y-motors in Fig. 10(b) increases linearly with ligand concentration due to the cooperative effect of two coupled Y-motors. This is quite different from the logarithmic increase of the average dwell time of a single Y-motor shown in Fig. 5(b) [solid line

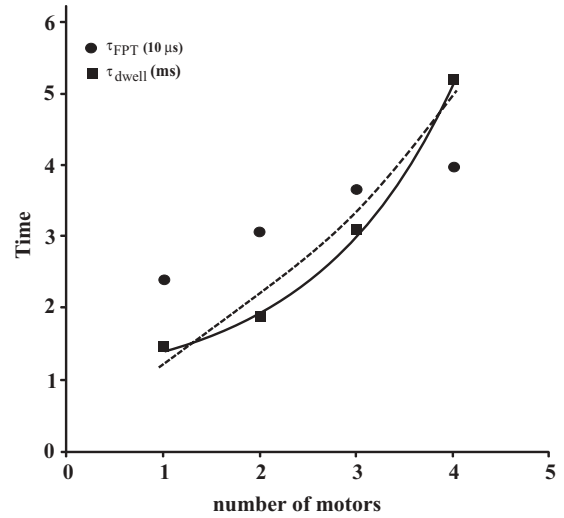


FIG. 11. Average first passage time (filled circles) and average dwell time (filled squares) for  $m$  coupled Y-motors where  $m$  increases from 1 to 4. The solid line shows an exponential fit of the average dwell time, while the dashed line is the best fit of the average dwell time using the formula  $(a^m - b)/m$  with  $a = 1.743$  and  $b = 1.232$ .

in Fig. 10(b)]. The comparison of  $\tau_{\text{FPT}}$  and  $\tau_{\text{dwell}}$  of a single motor with those of two coupled motors in Fig. 10 suggests that the speed of processive motion of motors is only slightly affected by the coupling, while the stability of processive motion is significantly enhanced in the limit of large ligand concentration.

To study the cooperative effects of coupled Y-motors further, we calculated both  $\tau_{\text{FPT}}$  and  $\tau_{\text{dwell}}$  for  $m$  coupled motors, where  $m = 2, 3$ , and 4. In Fig. 11, it is shown that the average first passage time of  $m$  coupled Y-motors increases slowly with  $m$ , while the average dwell time increases rapidly with  $m$ . To clarify the dependence of  $\tau_{\text{dwell}}$  on  $m$ , we fit our data of  $\tau_{\text{dwell}}$  with an exponential curve (solid line) and the curve of  $(a^m - b)/m$  derived from a recent theoretical prediction of the average walking distance of  $m$  coupled cytoskeletal motors (dashed line) [6]. With our available data, the average dwell time of  $m$  coupled motors is better fit by the exponential curve for  $m \leq 4$ . The difference between these two curves is not significant for  $m \leq 10$ , but becomes noticeable for  $m \gg 10$ . Therefore, for  $m \leq 10$ , the generic feature of cooperative transport by several molecular motors is similar although the fundamental mechanism for motors walking along a track is quite different in our model in comparison with that for cytoskeletal motors of reference [6]. For any realistic application of our model motors, it is desirable that the average first passage time be as short as possible and the average dwell time be as long as possible. The characteristic time scales found in Fig. 11 for  $m$  coupled motors therefore suggest that a train of molecular motors could be designed to transport cargoes.

### V. CONCLUSIONS

In this work, we proposed a simple model for studying the processive motion of single and coupled synthetic protein motors along a DNA track. MC simulations were carried out

to investigate their processive dynamics. Although an absolute measure of physical time is not provided in MC simulations, we calibrate the MC time unit (one MC step) by measuring the self-diffusion coefficient of a Y-motor in solution from both MC simulations and Langevin dynamics simulations, which gives one MC step  $\sim 25$  ps in two dimensions and 27 ps in three dimensions. The processive motion of motors along the DNA track is controlled by a time series of bulk ligand pulses ( $l_A, l_B, l_C$ ). We investigated  $\tau_{\text{FPT}}$  and  $\tau_{\text{dwell}}$  by varying the ligand concentration  $[N]$  as well as the effective range  $\xi$  and the strength  $V_0$  of the binding interaction between motors and the track. For single motors, it was found that  $\tau_{\text{FPT}}$  decreases logarithmically with  $[N]$ , while  $\tau_{\text{dwell}}$  increases logarithmically with  $[N]$ . It was furthermore found that  $\tau_{\text{FPT}}$  increases as  $\xi$  decreases and saturates for small values of  $\xi$ . The value of  $\tau_{\text{dwell}}$  increases with  $\xi$  for  $\xi < 2.21$  nm and  $\xi > 3.83$  nm but decreases significantly with  $\xi$  for  $2.21 \text{ nm} < \xi < 3.83$  nm. Our simulation results also show that  $\tau_{\text{FPT}}$  decreases exponentially with  $V_0$  for  $V_0 < 10k_B T$  and reaches a constant value for  $V_0 > 10k_B T$ , while  $\tau_{\text{dwell}}$  increases exponentially with  $V_0$  for  $V_0 < 10k_B T$  and saturates at  $V_0 \cong 100k_B T$ .

The examination of the processive dynamics of coupled motors is the principal aim of this work. For two coupled motors with a coupling strength  $k$ , the coupling between neighboring motors tends to increase the value of  $\tau_{\text{FPT}}$  logarithmically. The value of  $\tau_{\text{dwell}}$  for coupled motors decreases logarithmically with  $k$  for  $k < 8.2$  pN/nm and increases linearly with  $k$  for  $k > 8.2$  pN/nm. In particular, we investigated the experimental conditions for robust processive motion of coupled motors, in which case the value of  $\tau_{\text{FPT}}$  is minimized and the value of  $\tau_{\text{dwell}}$  is maximized. Our MC simulations for coupled motors show that, by increasing ligand concentration, the value of  $\tau_{\text{FPT}}$  for coupled motors is similar to that of single motors, but the value of  $\tau_{\text{dwell}}$  for coupled motors is much larger than that of single motors. Furthermore our simulations of  $m$  coupled motors show that  $\tau_{\text{FPT}}$  only increases slowly with  $m$  whereas  $\tau_{\text{dwell}}$  increases exponentially with  $m$ . These characteristic time scales for  $m$  coupled motors suggest that a train of molecular motors could be designed to transport cargoes over larger distances than for single motors. We plan to extend the work in this paper to the case when the coupled TWs are completely flexible in 3D.

#### ACKNOWLEDGMENTS

This work is supported in part by the National Science Council of Taiwan under Grant No. NSC 97-2112-M-003-005 -MY2. We wish to thank the IRMACS Centre at Simon Fraser University for their hospitality and the use of their

facilities. CMC wishes to thank Michael Plischke for his support and stimulating discussions at Simon Fraser University. M.J.Z. wishes to thank the NSERC of Canada and the Human Frontiers Science Project for Synthetic Protein Motors (HFSP-SPM) for financial support and his colleagues in the HFSP-SPM for numerous helpful and stimulating discussions regarding the TW.

#### APPENDIX

The Langevin simulations used to calculate the diffusion coefficient of the single rigid TW are identical in method to those used by Kuwada *et al.* [10]. In brief the over-damped discretized Langevin equation can be written as follows. Let  $\Delta x_i^{(j)}$  be the change in the value of the  $i$ th coordinate of the  $j$ th monomer of the TW in increment  $\Delta t$  at time  $t$ . Here  $i$  ( $=1$  to 3) are coordinate indices,  $j = 1(A')$ ,  $2(B')$ , and  $3(C')$ , for the repressor ‘‘feet’’ of the TW and  $j = 4$  for the hub. The Langevin equation can then be written as

$$\Delta x_i^{(j)} = F_i^{(j)} \Delta t / \gamma + (2k_B T \Delta t / \gamma)^{1/2} \xi_i^{(j)}. \quad (\text{A1})$$

In Eq. (A1)  $F_i^{(j)}$  is the  $i$ th component of the force on the  $j$ th monomer at time  $t$ ,  $\gamma$  is the drag coefficient for each monomer, and  $\xi_i^{(j)}$  is a Gaussian random number. Assuming that the monomers (repressors) are spheres of radius 2 nm [10] and using the viscosity of water at room temperature, Stokes’ law gives  $\gamma = 1.2\pi \cdot 10^{-11}$  kg/s. The force  $F_i^{(j)}$  acting on each monomer is derived from the following potential:

$$V = V_H + V_b. \quad (\text{A2})$$

$V_H$  is a harmonic potential which fixes the length of the bonds between the hub and the three feet of the TW and is given by

$$V_H = k_H \sum_i (|\mathbf{r}_4 - \mathbf{r}_i| - L)^2 / 2. \quad (\text{A3})$$

Here,  $\mathbf{r}_4$  is the position vector for the hub,  $\mathbf{r}_i$  is the position vector for the feet ( $i = 1$  to 3) and  $L = 7$  nm is the bond length. We take  $k_H = 16k_B T/\text{nm}^2$ . The bending potential  $V_b$ , which maintains the angle between neighboring bonds of the TW at close to  $120^\circ$ , is given by

$$V_b = k_b \sum_{i,i'} \{1 - \cos(\vartheta_{i,i'})\} \quad (\text{A4})$$

Here  $\vartheta_{i,i'}$  is the angle between neighboring bonds  $i$  and  $i'$ . We take  $k_b = 2000k_B T$ . The values of the self-diffusion constants for the single TW in two and three dimensions were found from the Langevin simulations to be  $D(2D) = 7.8 \times 10^{-12}$  m<sup>2</sup>/s and  $D(3D) = 6.7 \times 10^{-12}$  m<sup>2</sup>/s, respectively.

- 
- [1] J. Howard, *Mechanics of Motor Proteins and the Cytoskeleton* (Sinauer, Sunderland, 2001).  
 [2] *Molecular Motors*, edited by M. Schliwa (Wiley-VCH, Weinheim, 2003).  
 [3] H. C. Berg, *Annu. Rev. Biochem.* **72**, 19 (2003).

- [4] A. B. Kolomeisky and M. E. Fisher, *Annu. Rev. Phys. Chem.* **58**, 675 (2007).  
 [5] S. Leibler and D. A. Huse, *J. Cell. Biol.* **121**, 1357 (1993).  
 [6] S. Klumpp and R. Lipowsky, *Proc. Natl. Acad. Sci. USA* **102**, 17284 (2005) and references therein.

- [7] E. B. Stukalin, H. Phillips, and A. B. Kolomeisky, *Phys. Rev. Lett.* **94** 238101 (2005) and references therein.
- [8] J. W. Driver, A. R. Rogers, D. K. Jamison, R. K. Das, A. B. Kolomeisky, and M. R. Diehl, *Phys. Chem. Chem. Phys.* **12**, 10398 (2010) and references therein.
- [9] E. H. C. Bromley, N. J. Kuwada, M. J. Zuckermann, R. Donadini, L. Samii, G. A. Blab, G. J. Gemmen, B. J. Lopez, P. M. G. Curmi, N. R. Forde, D. N. Woolfson, and H. Linke, *HFSP J.* **3**, 204 (2009).
- [10] N. J. Kuwada, M. J. Zuckermann, E. H. C. Bromley, R. B. Sessions, P. M. G. Curmi, N. R. Forde, D. N. Woolfson, and H. Linke, *Phys. Rev. E* **84**, 031922 (2011).
- [11] N. J. Kuwada, G. A. Blab, and H. Linke, *Chem. Phys.* **375**, 479 (2010).
- [12] J. Carey, *Proc. Natl. Acad. Sci. USA* **85**, 975 (1988).
- [13] K. L. B. Borden, P. Beckmann, and A. N. Lane, *Eur. J. Biochem.* **202**, 459 (1991).
- [14] P. H. von Hippel, A. Revzin, C. A. Gross, and A. C. Wang, *Proc. Natl. Acad. Sci. USA* **71**, 4808 (1974).
- [15] K. Binder and D. W. Heermann, *Monte Carlo Simulation in Statistical Physics: An Introduction* (Springer, Heidelberg, 2010).
- [16] K. Binder, *Rep. Prog. Phys.* **60**, 487 (1997).
- [17] H. E. A. Huitema and J. P. van der Eerden, *J. Chem. Phys.* **110**, 3267 (1999).
- [18] V. I. Manousiouthakis and M. W. Deem, *J. Chem. Phys.* **110**, 2753 (1999).
- [19] H. Xu, M. Moraitis, R. J. Reedstrom, and K. S. Matthews, *J. Biol. Chem.* **273**, 8958 (1998).
- [20] I. Saint-Girons, J. Belfaiza, Y. Guillou, D. Perrin, N. Guiso, O. Bârzu, and G. N. Cohen, *J. Biol. Chem.* **261**, 10936 (1986).
- [21] K. D. Powell, S. Ghaemmaghami, M. Z. Wang, L. Ma, T. G. Oas, and M. C. Fitzgerald, *J. Am. Chem. Soc.* **124**, 10256 (2002).